

Direct Mapping of Local Seebeck Coefficient in 2D Material Nanostructures via Scanning Thermal Gate Microscopy

Achim Harzheim¹, Charalambos Evangelis¹, Oleg V. Kolosov^{3*}
and Pascal Gehring^{1,2*‡}

¹ Department of Materials, University of Oxford, Oxford OX1 3PH, United Kingdom

² Department of Physics, Lancaster University, Bailrigg, LA1 4YB, Lancaster, United Kingdom

³ Kavli Institute of Nanoscience, Delft University of Technology, Delft 2628, Netherlands

E-mail: o.kolosov@lancaster.ac.uk, pascal.gehring@imec.be

Abstract. Studying local variations in the Seebeck coefficient of materials is important for understanding and optimizing their thermoelectric properties, yet most thermoelectric measurements are global over a whole device or material, thus overlooking spatial divergences in the signal and the role of local variation and internal structure. Such variations can be caused by local defects, metallic contacts or interfaces that often substantially influence thermoelectric properties, especially in two dimensional materials. Here, we demonstrate Scanning Thermal Gate Microscopy (STGM), a non-destructive method to obtain high resolution 2-dimensional maps of the thermovoltage, to study graphene samples. **We demonstrate the efficiency of this newly developed method by measuring local Seebeck coefficient in a graphene ribbon and in a junction between single-layer and bilayer graphene.**

Increasing the efficiency of thermoelectric materials is necessary to enable devices that could scavenge waste heat and convert it into useful electrical energy. This is particularly true as current bulk thermoelectric generators lack the required conversion capability to be competitive with everyday heat engines such as standard combustion engines [1]. In addition, knowledge about the thermoelectric properties of materials and devices can reveal fundamental physical characteristics [2] or be used to design novel temperature sensors [3] and increase device efficiency in e.g. photovoltaic/thermoelectric hybrid structures [4]. While global thermoelectric measurements, that is measuring the voltage drop over a sample in response to an applied temperature gradient, are common, they cannot reveal the local variations of the thermoelectric properties in the sample. Yet, it has been shown that metal contacts [5], defects and other localized effects [6, 7] can impact the local thermoelectric characteristics drastically. Thus, it is important to apply a method to study local trends in materials and devices but only

‡ Present address: IMEC, Kapeldreef 75, 3001 Leuven, Belgium.

few attempts have been made as of today. Here we demonstrate Scanning Thermal Gate Microscopy (STGM), a novel non-destructive method to readily probe the local thermoelectric properties of devices made of 2D and thin film materials with few tens of nm lateral resolution. Similar to an atomic force microscope, this technique allows the repeated measurement of the local thermovoltage response without impacting the device structure or changing the transport properties. Local mapping has been reported using SThM techniques previously, yet these techniques require an electrical contact between a conducting SThM tip and the sample thus adding a major variability in thermoelectric measurements [8, 9]. In a previous report we described a measurement to probe the AC Peltier, Joule and thermovoltage of a sample. However, the new STGM method presented in the current manuscript has several key advantages compared to our previous approach: by employing a direct DC heating approach to only measure the thermovoltage, STGM enables a higher resolution, exclude phase driven effects and, essentially, makes it possible to quantitatively estimate the Seebeck coefficient through deconvolution. Furthermore, other than the previous method, the technique presented in this work does not require the use of multiple lock-in amplifiers (and therefore avoids the corresponding long integration times), which substantially increases the achievable scanning speed and makes the method readily applicable for any SThM setup. Another attempt at the local measurement of thermoelectric effects was made via photocurrent measurements, including for devices similar to those studied here [10, 11]. However, laser spot sizes tend to be in the μm range, the temperature increase caused by the laser can typically only be simulated with finite element analysis and the technique is inherently measuring a mix of photo thermoelectric and photovoltaic effects [12, 13].

Local scanning methods can necessarily only probe the surface of materials, making two dimensional (2D) materials an ideal test bed for localized thermoelectric measurements. In addition, 2D materials allow to readily tune their electronic properties via a back-gate, have an inherent control over their layer thickness and exhibit an ordered crystalline structure. 2D materials are also particularly promising as they have the potential to be integrated on a wafer scale basis [14, 15] or to be incorporated into current CMOS technology [16]. Graphene is the most-studied material out of the 2D family, and its thermoelectric properties can be influenced by gating [17, 18], local charge carrier fluctuations [19], introduction of nanoparticles [20] or increased scattering at the edges [21]. Yet, the thermoelectric properties of graphene have mostly been studied globally or in combination with photocurrent measurements.

In this study we demonstrate STGM for multiple graphene devices, imaging local thermoelectric phenomena at varying carrier concentrations. We first image a rectangular graphene strip as a function of gate voltage and secondly a more complex single-layer/bilayer graphene (SLG/BLG) junction device. Using STGM, we are able to resolve the impact of metallic contacts, changes in layer thickness and internal strain in the graphene and can quantify the length scales involved with changes in the Seebeck coefficient due to different causes. While the novel method is applied to graphene devices here, it is generally suitable for any 2D or thin film device structure.

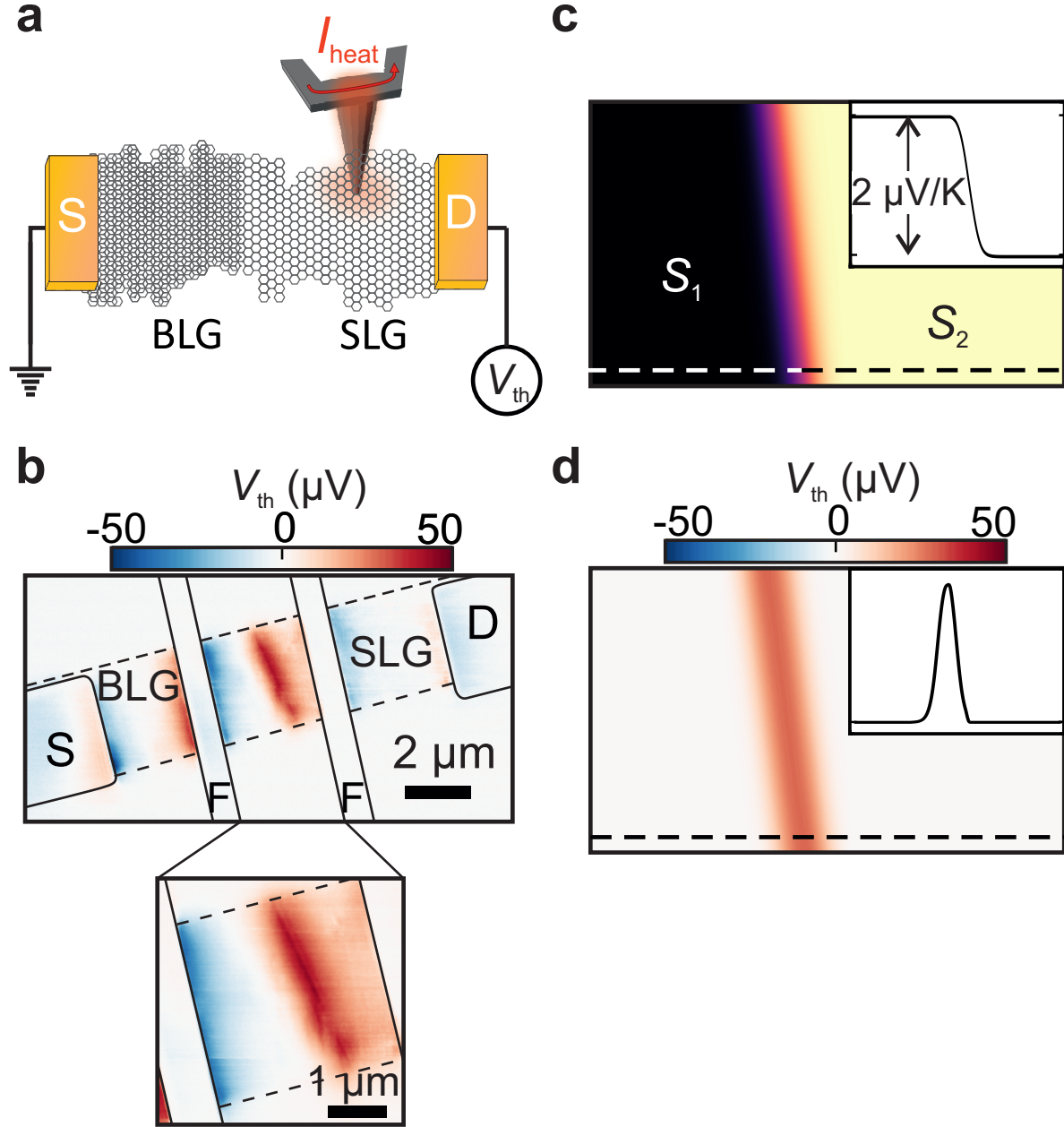


Figure 1. (a) Schematic of the STGM measurement setup. (b) Exemplary thermovoltage map of a SLG/BLG junction. The thermovoltage is measured between the source (S) and drain (D) contact with the other two contacts left floating (F). The dashed black lines indicate the position of the graphene flake and the black drawn through line the gold contacts. (c) Simulated Seebeck signal going from S_1 to S_2 , resulting in $\Delta S = 2 \mu V/K$. The inset shows a line trace through the Seebeck map with the position of the cut indicated by the dashed line. (d) Calculated thermovoltage map. The thermovoltage map was obtained by convoluting the Seebeck map in c) with the temperature distribution $dT(x)$ (see SI). The inset shows a line trace through the thermovoltage map with the position of the cut indicated by the dashed line.

Results and discussion

Our devices are made from exfoliated single-layer and bilayer graphene top contacted by Ti-Au contacts on a Si/SiO₂ chip that serves as a global back gate (see methods for fabrication details). The measurements are performed employing a Scanning Thermal Microscope (SThM) setup, effectively an atomic force microscope (AFM) with a microfabricated resistor incorporated on the cantilever of the AFM probe close to the tip [22]. When applying a high DC or AC voltage to the resistor the tip can be heated up by tens of Kelvin above the ambient SThM temperature and used as a local heat source. As this heat source is scanned over the sample with nanometer precision, the position dependent open-circuit voltage drop on the device is recorded (see Figure 1a for the measurement schematic) and in equilibrium no current is flowing in the sample. STGM effectively presents a three terminal probing technique where heat from the STGM tip modifies the potential voltage drop across the two electrical terminals, producing a 2D nanoscale map of the thermoelectric response. Crucially, STGM does not require an electrical contact between the tip and the probed sample to measure the local thermoelectric response.

For a given Seebeck coefficient $S(x)$ and a temperature increase caused by the tip $T(x)$, the tip position dependent thermovoltage can be written as (see SI)

$$V_{\text{th}}(x_{\text{T}}) = - \int_{x_{\text{L}}}^{x_{\text{R}}} S(x) \frac{\partial T(x - x_{\text{T}})}{\partial x} dx. \quad (1)$$

Here x_{T} denotes the position of the tip, x_{L} and x_{R} the position of the left and right contact and $\frac{\partial T(x - x_{\text{T}})}{\partial x}$ the position dependent derivative of the temperature profile caused by the hot tip. Assuming that $T(x)$ is a symmetric function, Equation (1) shows that V_{th} reflects the local variations (asymmetry) of $S(x)$ around x_{T} within a length scale given by the thermal resistances of the sample. For a SLG/BLG junction for example, where symmetry is broken by the SLG/BLG step, we observe a positive thermovoltage signal at the junction when measuring the voltage drop at the SLG contact with the BLG contact grounded as shown in Figure 1b. The adjacent additional signal caused by the contacts will be discussed later. This positive thermovoltage signal can be explained by two different Seebeck coefficients in the single-layer and bilayer graphene area of the device, respectively, due to the different energy dispersion at low energies as previously reported [11]. Assuming a device where two materials with different Seebeck coefficients S_1 and S_2 are connected we can calculate the expected thermovoltage signal by convoluting $S(x)$ with dT/dx as shown in Equation (1). The difference in Seebeck coefficient $\Delta S = S_2 - S_1 = 2 \mu\text{V/K}$ is displayed in Figure 1c. Here the temperature distribution is assumed to have a Gaussian shape see ([23] and SI) and we convolute each line of the Seebeck map with the temperature distribution to obtain the thermovoltage map. As can be seen in Figure 1d, the resulting thermovoltage signal is positive along the position of the junction where the BLG changes to SLG, reproducing the experimentally observed

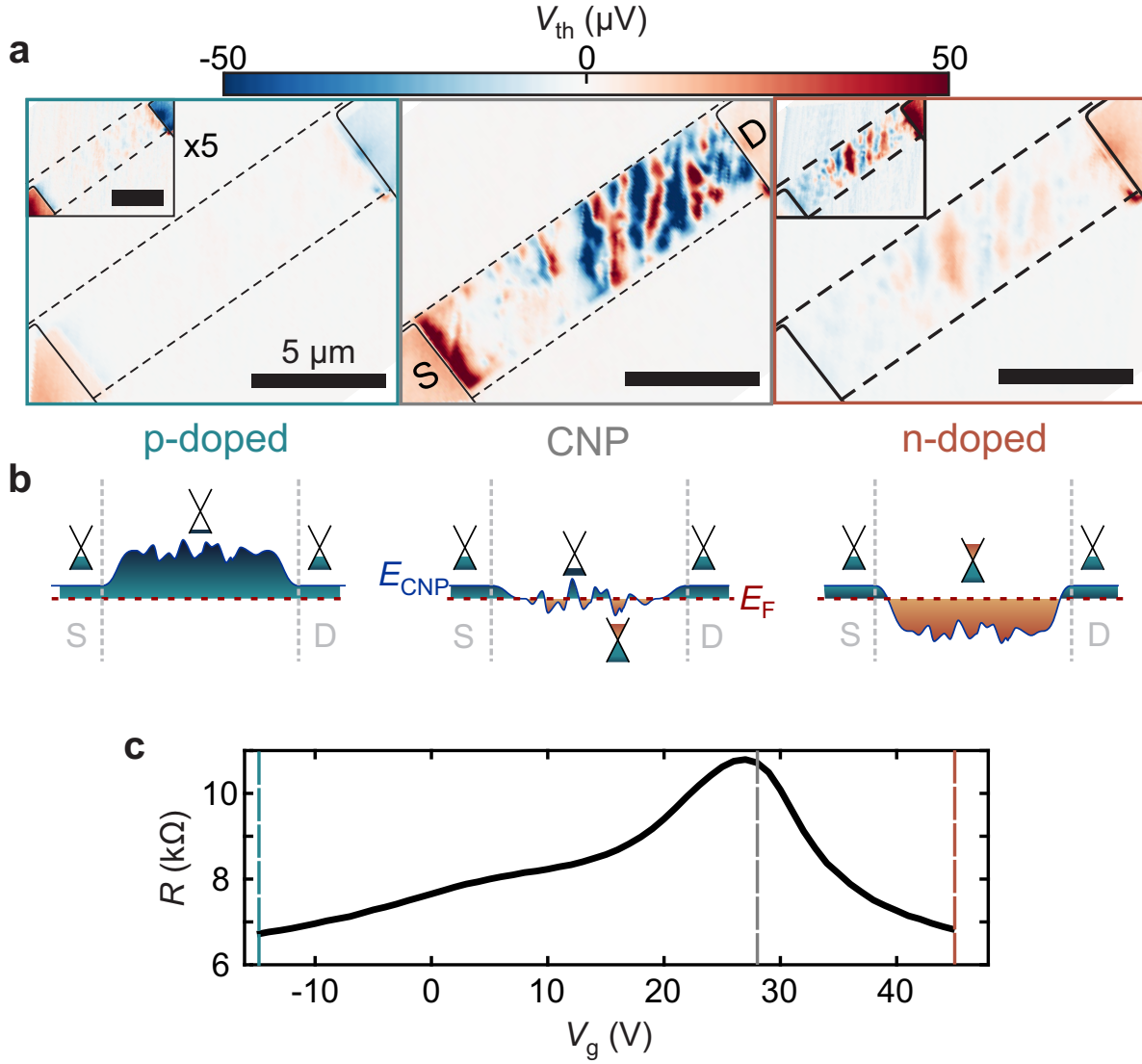


Figure 2. (a) Thermovoltage maps at three different gate voltages. The insets show the same map at a sensitivity of V_{th} -10 to 10 μV and all scale bars denote 5 μm . The dashed black lines indicate the position of the graphene flake and the black drawn through line the gold contacts. (b) Schematic showing the energy distribution in graphene relative to the Fermi energy band bending at the gold covered graphene to the graphene channel interface for a p-doped (left) and n-doped (right) graphene channel and at the charge neutrality point or CNP (middle). (c) Gatetrace of the device, showing the CNP point around 28 V. The dashed lines indicate the three gate voltages at which the above maps were recorded.

results well. We note that the width of the thermovoltage peak in the thermovoltage map is given by the length scale on which the change in Seebeck coefficient from S_1 to S_2 happens, and the width of the temperature distribution (see SI). As discussed later, it is possible to extract the width of the temperature distribution from the thermovoltage maps, which yields information about the band bending when changing the graphene thickness.

Rectangular Graphene Device

We first measure the gate dependent local thermoelectric signal of a graphene rectangle (see Figure 2). The charge neutrality point of the sample is at a back gate voltage of around $V_g = 28$ V, as inferred from the gate dependent measurement of the two-terminal channel resistance (see Figure 2c). Thus, the graphene is strongly p-doped at $V_g = 0$ V, which is due to the interaction of the SiO_2 substrate surface charges with the graphene as reported previously [24, 25]. An STGM thermovoltage map with a tip apex-temperature of $T_{\text{tip}} \approx 53$ K is recorded at three back gate voltages: for a p-doped graphene channel at -15 V, close to the Dirac point at 28 V and for an n-doped graphene channel at 45 V (Figure 2a, left to right). The tip-apex temperature is defined with respect to the microscope stage and when the tip is in contact with the sample surface. In the p-doped regime, a thermovoltage on the order of 30 μV is generated across the device when the hot tip heats up the areas around the electrical contacts, where the polarity of the induced thermovoltage is negative (positive) when the source (drain) is locally heated up. As before, the source is defined as the contact kept on ground during the measurement. Only very little to no thermovoltage drop is observed when the tip is scanned over the graphene channel. At low carrier concentrations around the Dirac point, a seemingly chaotic distribution of thermovoltage signal of changing polarity appears in the graphene channel. In the n-doped regime, the signal along the graphene strip is again reduced. A larger voltage build up (compared to that in the channel) is observed when the source and drain contacts are heated up, with opposite polarity compared to the p-doped case.

The chaotic signal observed close to the Dirac point is attributed to charge puddles inside the graphene channel, which locally vary the energy dependent position of the charge neutrality point and are commonly observed for graphene on SiO_2 substrates (see Figure 2b) [19, 26]. This leads to sharp local variations in S which in turn influences the thermovoltage signal. We note that the signal from the charge puddles dominates the map at the charge neutrality point. This is due to the high sensitivity of the magnitude and sign of the Seebeck coefficient on the carrier density around the Dirac point [19, 17], resulting in large differences in S over the short distances associated with charge puddles.

It is important to note, that a change in the thermal spreading resistance of the sample and the tip-sample interface thermal resistance, which is dominated by the thermal conductivity of the measured surface, strongly influences the tip-apex temperature. This is particularly relevant when the hot tip is in contact with the Au electrodes since the thermal conductivity of Au is two orders of magnitude larger than that of SiO_2 /graphene on SiO_2 . This leads to a reduction of the excess tip-apex temperature from $T_{\text{tip}} \approx 53$ K to $T_{\text{tip}} \approx 1.5$ K when the tip is in contact with Au compared to SiO_2 /graphene [27].

In the following we discuss the origin of the observed thermovoltage signals. When the hot tip heats up the left or right electrical contact, the measured thermovoltage drop

corresponds to the sum of the thermoelectric voltage build-up of the graphene under the Au contacts and the graphene channel. This signal will later be used to estimate the (global) Seebeck coefficient of the graphene channel with respect to the graphene underneath the contact [5].

The origin of thermoelectric signals is the preference of charge carriers to diffuse from hot regions in a material towards colder regions. The driving force for this process is proportional to the temperature difference ΔT and the entropy the system gains per diffusing carrier. The latter is highest if a carrier diffuses towards regions of higher DOS. This, depending on the source/drain configuration and the majority carriers in the sample, results in the build up of a positive or negative thermovoltage under open circuit conditions.

Graphene underneath the gold contacts is shielded from the electric field created by a gate voltage, such that its carrier concentration is not affected when a V_g is applied. For a gate voltage $V_g = 45$ V, where the graphene channel is highly n-doped (see Figure 2a right) the DOS at the Fermi energy is larger in the channel than in the graphene underneath the gold contact (see Figure 2b right), meaning electrons will diffuse from the contact area into the graphene channel. This results in a positive (negative) thermovoltage build up at the drain (source) contact. While the DOS in the channel is still larger in the channel than in the graphene underneath the gold contact for a p-doped sample (see Figure 2b left), the majority carriers are now holes, resulting in a negative (positive) thermovoltage build up at the drain (source) contact.

Single-layer/Bilayer Junction

In the following, we apply STGM to a second type of graphene device, a junction formed between SLG and BLG (similar to the device and measurement shown in Figure 1b). Shown in Figure 3, the sample consists of a graphene flake that has both a single-layer and a bilayer section and is contacted by four gold contacts. The two contacts labelled source (S) and drain (D) are used for measuring the thermovoltage drop, while the other contacts are left floating (F).

In Figure 3, in accordance with the previous measurement of the graphene rectangle, a thermovoltage signal on the contacts is observed, which switches polarity as the gate voltage is swept over the charge neutrality point. The gate dependent thermovoltage maps highlight the impact of the contacts on the graphene sample.

The two passive, floating contacts show bi-polar signals, reversing polarity as the gate voltage is increased. This is because the floating contacts locally dope the graphene and pin the carrier density, an effect that has previously been observed in scanning photocurrent microscopy measurements [28]. In addition, the Fermi level pinning from the contacts leads to a strongly non-homogenous change of the carrier density within the sample. Rather than occurring simultaneously over the whole sample area, the change is gradual, starting from the SLG/BLG junction and wandering out towards the contacts as can be seen for higher gate voltages (right side of Figure 3 and further

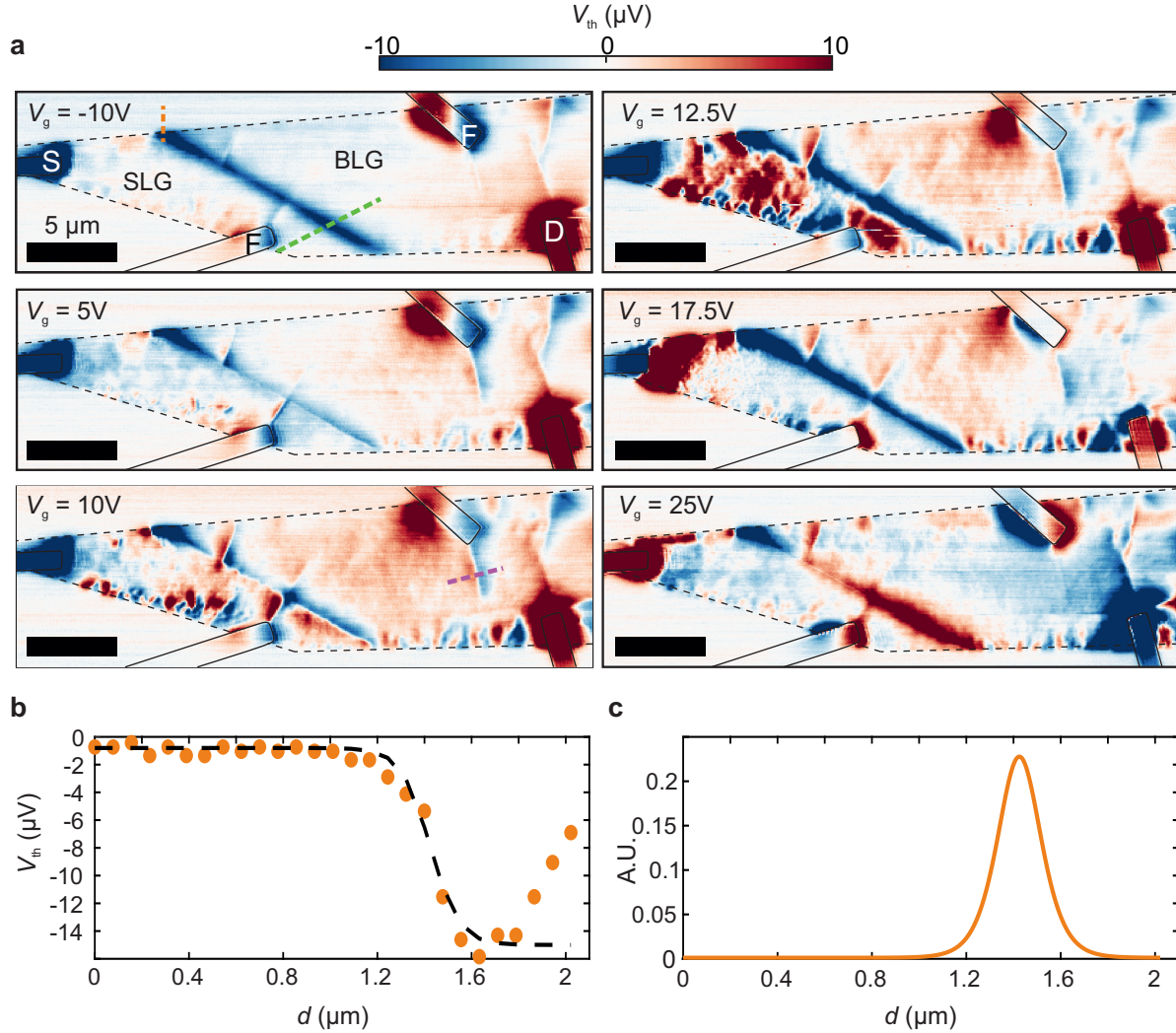


Figure 3. (a) Thermovoltage maps at six different gate voltages for a SLG and BLG graphene flake. The source and drain contacts are indicated by S and D respectively and the positions of the line traces analysed later are indicated by the green dashed line in the top left and the pink dashed line in the bottom left image. The dashed black lines indicate the position of the graphene flake and the black drawn through the gold contacts. All scale bars denote $5 \mu m$. (b) Linecut indicated in the top left panel in a) by the orange dotted line (orange dots) and a sigmoidal Boltzmann curve fit (black dotted line). (c) Derivative of the fit in b).

images in the SI). Furthermore, STGM allows us to image the gate screening due to a second layer of graphene on top of the SLG channel. While a multitude of charge puddles appear around the charge neutrality point for gate voltages $V_g = 10/12.5$ V on the SLG side, the BLG area of the sample shows hardly any. This is attributed to the electric field created by surface dipoles in the oxide being screened by the bottom layer and consequently not affecting charge carriers in the top layer, as previously indirectly observed [29, 30]. In addition, this observation provides evidence that the two graphene layers are thermally largely decoupled [31]. Assuming charge puddles are present in the

bottom layer as they are in the SLG area, any temperature differential caused by the tip should cause a thermovoltage signal, which is not observed in our experiment.

Furthermore, we observe thermovoltage signals along straight lines (one example is highlighted by a pink dashed line in the bottom left panel of Figure 3a) which are not visible in the height topography AFM maps (see SI). This signal could be attributed to local strain in the graphene layer or wrinkles, induced by the deposition of the contacts or the annealing step. Strain has been shown to alter the band structure [32] and Seebeck coefficient in graphene as well as displaying a Peltier effect [33]. Notably, at all gate voltages a strong thermovoltage signal is observed when heating up the interface between SLG and BLG as reported in scanning photocurrent measurements [10, 11]. The signal is changing from negative to positive as the gate voltage is increased. Both the wrinkle and the SLG/BLG junction signal follow a non-linear gate dependence.

The change in the sign at the SLG/BLG interface with changing majority carrier concentration (here both the SLG and BLG area of the sample is assumed to be p-doped (n-doped) for low (high) gate voltages respectively) implies that there is a change in the Seebeck coefficient difference $\Delta S = S_{\text{SLG}} - S_{\text{BLG}}$.

As discussed above, diffusion of carriers is driven by a gain in entropy, and carriers diffuse from regions of low DOS into regions of high DOS. Due to the parabolic dispersion relation in BLG compared to the linear one in SLG around the charge neutrality point, the DOS in BLG is higher than in SLG [34, 35]. This leads to a positive (negative) thermovoltage build-up for electron (hole) doped graphene when measuring the voltage at the drain contact with respect to the source [11]. This development is shown in Figure 4a where line traces along the green dotted line in Figure 3a through the junction at different gate voltages are displayed. Figure 4b, top, shows close ups of the position dependent thermovoltage signal for a high p-doped ($V_g = -10$ V) and n-doped ($V_g = 25$ V) sample. For p-doped (n-doped) graphene, the signal dips (peaks) at the interface between SLG and BLG. Such a dip (peak) observed for the highly p-doped (n-doped) sample, respectively, is predicted by the model presented in Figure 1 and can be attributed to a step-wise change in the Seebeck coefficient between the SLG and BLG areas.

However, at gate voltages close to the charge neutrality point of the sample ($V_g = 10/12.5$ V) the thermovoltage exhibits a bipolar signal not compatible with a Seebeck coefficient changing from S_1 to S_2 . A similar bipolar signal at $V_g = 10$ V is found around wrinkles as shown for an exemplary linecut in Figure 4c. Rather than indicating a transition from one Seebeck coefficient value to another, a bipolar signal implies a drop/peak of the Seebeck coefficient (see SI for simulations similar to the ones shown in Figure 1). For the wrinkles, the sudden spatial change in the Seebeck coefficient can be explained by local strain, which is the origin of the fold or wrinkle formation in the first place. It has been predicted that local strain in graphene can alter its Seebeck coefficient with the magnitude of this effect being largest around the charge neutrality point [36]. As a result, wrinkles in graphene exhibit a bipolar and prominent signal around the CNP. At higher doping, the change in the Seebeck coefficient is not as large

and only leads to a small ΔS . While this describes the signal at the wrinkles, the nature of the bipolar thermovoltage displayed at the SLG/BLG junction is less clear. The bipolar thermovoltage could be a combination of the signal from charge puddles and the junction or be attributed to local symmetry breaking and disorder at the edges of the BLG which locally influences the Seebeck coefficient.

As explained above, the magnitude of the local thermovoltage signal measured by STGM is given by a convolution of a temperature difference with a given spatial Seebeck coefficient distribution. Thus it is possible to extract the length scales the Seebeck coefficient is changing on associated with the different origins of the signals. We note that the spatial distribution in the thermovoltage signals is directly influenced by two factors: the shape and height of the temperature profile distribution created by the STGM tip and the local changes of the Seebeck coefficient. In order to determine the width of the temperature distribution created by the STGM tip, we fit the step in the thermovoltage signal at the graphene flake edge with a sigmoidal Boltzmann curve $f(x) = y_1 + (y_1 - y_2)/(1 + e^{\frac{x-x_0}{\Delta x}})$ (see orange dashed line in the top left pannel in Figure 3a and SI) [37]. This fit gives $\Delta x \approx 60\text{nm}$, suggesting a lateral resolution of $2\Delta x = 120\text{nm}$. From this fit we can also extract a width of the Gaussian temperature distribution of $l_{dT} \approx 1 \mu\text{m}$ (see SI).

By comparing l_{dT} to the length scales observed in the experiment for the thermovoltage signal, $l_V \geq 3 \mu\text{m}$ (see Figure 4b and c), it becomes clear that the width of the signal can not be explained by limited spatial resolution. Since the thermovoltage signal measured is a convolution of S and dT , the signal width is approximately given by the sum of l_{dT} and l_S (the length scale associated with changes in the Seebeck coefficient), making it possible to extract l_S . The signal width can then be used to quantify the band bending at the transition between SLG to BLG (similarly to the depletion region width in a semiconductor p-n junction that is determined by doping levels and applied voltage). Applying this to the line traces shown in Figure 4a which show $l_V \approx 3 \mu\text{m}$, we can extract the length scale of the Seebeck coefficient transition when moving from SLG to BLG, giving $l_S \approx 2 \mu\text{m}$ for both a p-doped and an n-doped sample. We note that our results suggest that l_S depends on the carrier density: by lowering the carrier density we find that l_S decreases to $l_S \approx 1 \mu\text{m}$ at $V_g = 5 \text{ V}$ (see Figure 4a and SI). It is worth to mention that, although the length scales on which the Seebeck coefficient changes around the SLG/BLG junction and a wrinkle are similar, the underlying mechanism for this length scale is different (see Figure 4b top and c). While l_S around the junction depends on charge carrier density, l_S for wrinkles in graphene is expected to depend more on the elastic properties of graphene. Thus the above analysis suggests that even for an atomically sharp step between two 2D materials, the Seebeck coefficient changes gradually on a length scale of micrometers.

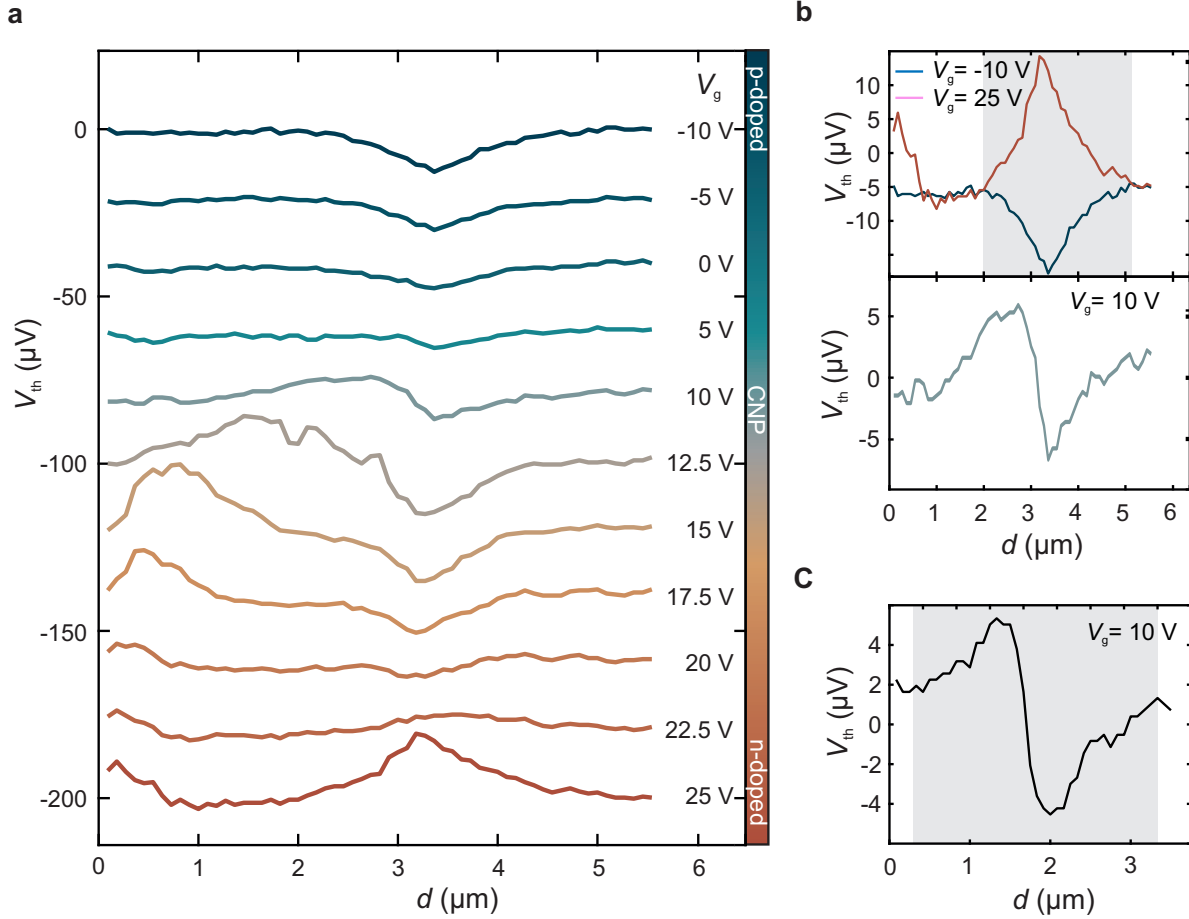


Figure 4. (a) Linetraces through the SLG/BLG junction device extracted from the previously measured thermovoltage maps for different gate voltages. The linetraces are offset by $-20 \mu\text{V}$ each for clarity. (b) Linetrace through the SLG/BLG junction at $V_g = -10 \text{ V}$ and $V_g = 25 \text{ V}$ showing a dip/peak (top) and at $V_g = 10 \text{ V}$ showing a bipolar signal (bottom). (c) Linecut through the thermovoltage signal of a wrinkle in the SLG/BLG sample. The grey shaded area indicates the width of the signal.

Estimating the Seebeck coefficient

Following Equation (1), the local thermovoltage is a convolution of the local variation of the Seebeck coefficient and the temperature gradient induced by the STGM tip. Therefore it is possible to extract the local Seebeck coefficient variations from a measurement of the local thermovoltage by deconvolution. We test this idea by making the following assumptions: 1) we assume a Gaussian distribution of the temperature profile induced by the heated tip, with $\sigma \approx 100\text{nm}$ as extracted from the sigmoidal Boltzmann curve fit (see SI). 2) we assume a constant thermal spreading resistance and therefore a constant tip-apex temperature. The error making this assumption is low if only the graphene channel is investigated and contact areas are neglected. 3) the thermovoltage is measured between two sample contacts in the x-direction and therefore contributions in the y-direction can be neglected (here we rotate the thermovoltage maps before performing the deconvolution).

From Equation (1) we know that V_{th} is the convolution of S and the position dependent derivative of the temperature profile caused by the hot tip $T'(x_{\text{T}})$, i.e. $V_{\text{th}}(x_{\text{T}}) = (S * T')(x_{\text{T}})$. Using the temperature distribution $T(x_{\text{T}})$, and thereby $T'(x_{\text{T}})$, we can then deconvolute Equation (1) and obtain an estimate of the Seebeck coefficient distribution along the sample, $S(x)$ (see SI). Using a regularized filter in combination with a constraint least-square restoration algorithm to perform the 1D deconvolution, a quasi two-dimensional temperature distribution is line-by-line deconvoluted with the thermovoltage map to produce the Seebeck map (see methods and SI).

As the tip is moved over the sample, the centre of its two-dimensional temperature distribution moves as well. Then, at every point of the thermovoltage map, a complete deconvolution of each line in the temperature distribution with the thermovoltage image gives a point in the deconvolution image.

The resulting deconvolution is shown in Figure 5a. First, we note that the signal on and around the contacts is not accurate as we assumed a constant excess temperature of the tip-sample contact (of $T_{\text{tip}} \approx 53$ K) for the deconvolution. This is not given on the Au contacts where the tip-sample contact temperature drops substantially as discussed earlier. Therefore, the areas of the Au contacts, which effectively show the difference in Seebeck coefficients between gold and graphene [38], do not necessarily have the right magnitude (see discussion below). The graphene channel in between the contacts however, satisfies assumption 2 and displays the expected change in the Seebeck coefficient from positive to negative with increasing gate voltage [17]. In addition, large local variations of the magnitude and sign of the local Seebeck coefficient are observed around the Dirac point (see Figure 5). These give rise to the thermovoltage signal shown in Figure 2a.

In order to evaluate the deconvolution method presented in this work, we can compare its result to the Seebeck coefficient of the graphene channel obtained via two additional methods: 1) using the gate dependent conductance data of the device and the Mott formula to estimate S [17] and 2) estimating the temperature drop ΔT over the whole sample when the STGM tip heats up one electrical contact, and use $S = V_{\text{th}}/\Delta T$. For case 1), the Mott formula is given by

$$S = -\frac{\pi^2 k_B^2 T}{3|e|} \frac{1}{G} \frac{dG}{dV_g} \frac{dV_g}{dE} \Big|_{E=E_F} , \quad (2)$$

where e is the electron charge, G the electrical conductance, k_B the Boltzman constant and T the operating temperature (see SI). The gate dependent Seebeck coefficient of the rectangular sample can then be calculated using the gatetrace from Figure 2c with the results of this calculation shown in Figure 5b. The calculated Seebeck coefficient overall first increases, changes sign when crossing the charge neutrality point, further decreases, and subsequently increases towards zero again. We observe maximum and minimum values of the Seebeck coefficient around $S = 30\text{-}40 \mu\text{V/K}$ and $S = -40$ to $-50 \mu\text{V/K}$, respectively.

Then, for method 2), we divide the average thermovoltage value on the contacts in

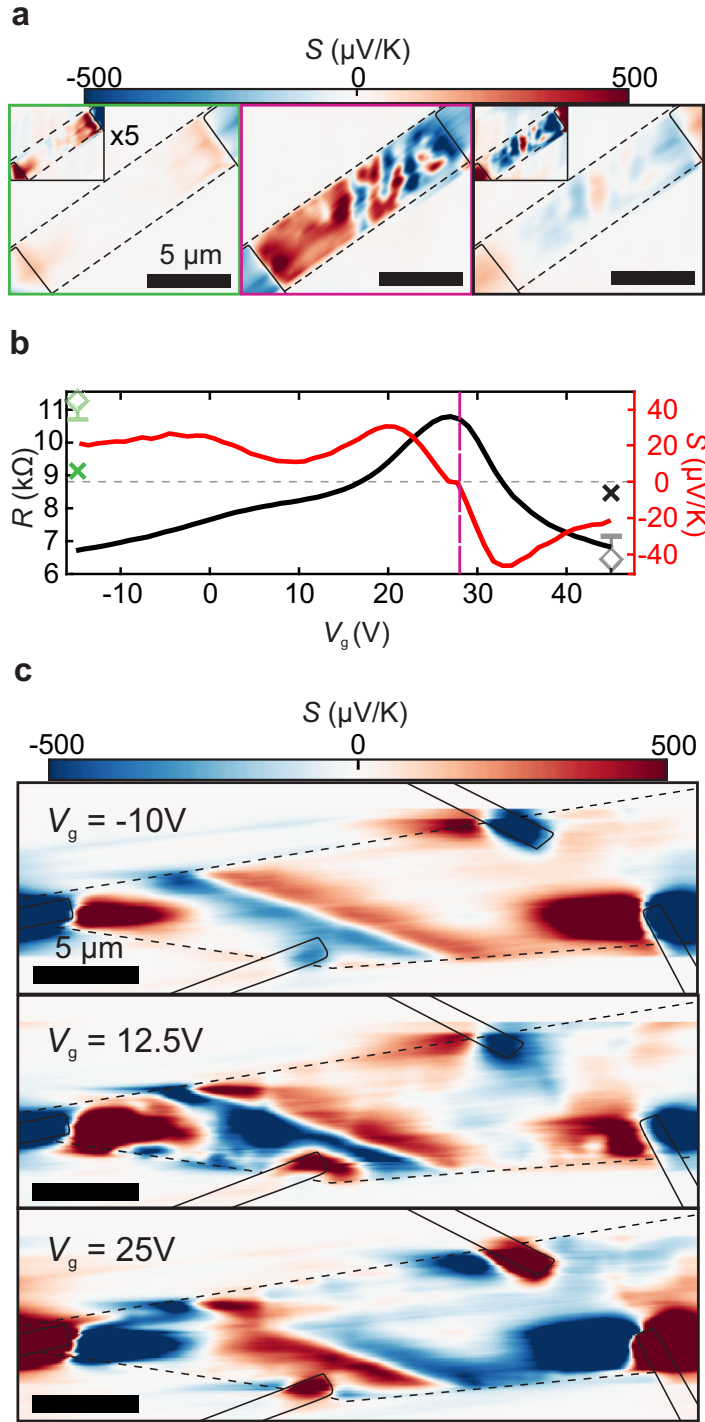


Figure 5. (a) Deconvolution of the thermovoltage maps of the rectangular graphene strip device. The insets show the same map at a sensitivity of S -20 to 20 $\mu\text{V/K}$. (b) Gate-trace of the rectangular device (black line), Seebeck coefficient calculated from Equation (2) (red line), Seebeck coefficient estimated from the thermovoltage maps (semitransparent diamonds) and the Seebeck coefficient extracted out of the deconvolution in a) (crosses). (c) Deconvolution of the thermovoltage maps of the SLG/BLG junction device. All scale bars denote 5 μm . The dashed black lines show the position of the graphene flake and the black drawn through line the gold contacts.

Figure 2a by the assumed temperature difference between the contacts (≈ 1.5 K as discussed) giving $S = 5.92 \pm 3.2 \mu\text{V/K}$ and $S = -4.19 \pm 1.49 \mu\text{V/K}$ for the Seebeck coefficient at low and high gate voltage respectively. The distribution of values of V_{th} on the contacts is plotted in a bar graph and fitted with a multi peaked Gaussian to determine the most likely event with the error then given by the width of the Gaussian (see SI).

Lastly, the Seebeck coefficient obtained via the deconvolution is extracted from the graphene channel in the maps of the spatial distribution of the Seebeck coefficient in Figure 5a. Again, the values of S in the channel are found by fitting the distribution with a multi peaked Gaussian to determine the most likely event with the error then given by the width of the Gaussian (see SI). This gives $S = 44.94 \pm 5.43 \mu\text{V/K}$ and $S = -42.91 \pm 9.4 \mu\text{V/K}$ for the p-doped and n-doped channel respectively. The result of the three different methods to obtain the Seebeck coefficient in the sample are shown in Figure 5b. The values found for all methods are qualitatively on the same order, considering the assumptions necessary and are in accordance with previously reported global thermovoltage measurements in graphene. In addition, all methods find the same trend of a reversal in sign when changing majority carriers as expected for graphene [17]. Method 2), that is the Seebeck coefficient estimated via the thermovoltage drop, quantitatively differs most likely due to the large error in determining the temperature difference across the device from heating up one contact. While this makes it difficult to quantify the Seebeck coefficient precisely, this is a well-known obstacle in every thermoelectric measurement and all estimates for the Seebeck coefficient presented here are consistent.

The deconvolution can also be applied to the more complex thermovoltage maps of the SLG/BLG sample (Figure 5c). Here, artefacts introduced by the changing tip-sample thermal resistance are clearly visible in the contact area. However, trends predicted by theory like the change in the Seebeck coefficient of the SLG area S_{SLG} with respect to the BLG area S_{BLG} are visible, with $S_{\text{SLG}} < S_{\text{BLG}}$ at $V_g = -10$ V and $S_{\text{SLG}} > S_{\text{BLG}}$ at $V_g = 25$ V [11]. In addition, again, a high local variation of S_{SLG} with changing polarity can be seen around the charge neutrality point, caused by charge puddles. While the calculated Seebeck coefficients around $500 \mu\text{V/K}$ may seem high for a graphene channel, we note that these are local variations due to local effects rather than representations of the global Seebeck coefficient.

Conclusions

To summarize, we have developed STGM, a method to probe the local thermoelectric properties of two-dimensional and thin-film devices on a nanometer scale. This method allowed us to observe the thermoelectric fingerprint of charge puddles in graphene, resolve effects in our sample such as Fermi level pinning by the metallic contacts leading to non-homogenous carrier concentration distribution and reveal how the local carrier concentration changes when a gate voltage is applied. Furthermore, we find that strain

strongly impacts the local Seebeck coefficient in single-layer and multilayer graphene sheets. The STGM method developed in this paper further allows us to obtain the local Seebeck coefficient through deconvolution. We find good qualitative agreement between values obtained by deconvolution and theory.

STGM is a valuable tool for future research on two-dimensional materials especially to noninvasively study planar junctions and the influence of local defects or metal contacts on the thermoelectric properties of the sample. This could provide important insights leading to new strategies to increase the efficiency of thermoelectric devices. In addition, further research into the thermoelectric signals in 2D materials will help to limit thermoelectric noise in electronic devices. STGM is not restricted to 2D materials but could also be applied to study the local thermoelectric properties around single molecule junctions or quantum dot devices [39, 40, 41].

Experimental

Device Fabrication. The devices were fabricated by exfoliating HOPG on top of a standard Si/SiO₂ chip with a 300 nm oxide layer. Subsequently, if required, the graphene was patterned employing standard electron-beam lithography and then etched using oxygen plasma. Then, 1 nm Ti/50 nm Au contacts were deposited on top of the graphene and the final devices were annealed at 350 degree Celsius under a forming gas atmosphere for 30 minutes.

Scanning Thermal Gate Measurements. The SThM is located in a high vacuum environment, prohibiting parasitic heat transfer as well as the formation of a water meniscus between the tip and the sample to achieve a better thermal resolution [42, 43]. In our measurements, the spatial resolution is limited by the size of the tip-sample contact, which is on the order of tens of nanometers.

For the STGM measurements, the SThM tip is heated up by applying a high AC voltage of $V_{heater} = 4 V_{pp}$ at a frequency of 91 kHz for the thermal conductance measurements with a 4 V DC offset to the temperature sensor. This causes Joule heating, which results in an SThM tip excess temperature of $T_{tip} \approx 53$ K at the interface with graphene on the SiO₂/Si substrate (see Supporting Information). This local heat source is then scanned over the sample while the global voltage drop V_{th} over the two contacts is measured with a SRS650 low-noise preamplifier and a SR560 high-impedance voltage preamplifier. The thermovoltage measurements do not require electrical contact between the tip and the sample, and thereby eliminate linked uncertainty, as well as requirements on the strength of the electrical tip-sample contact [44]. The SThM can also be used in a passive tip configuration with the temperature of the sample modified via cooling (heating) of the stage.

We calibrate the electrical power applied to the tip resistor as a function of temperature on a heated stage inside a high-vacuum chamber as described elsewhere [27, 45]. Crucially, here the tip apex temperature is a fraction of the cantilever temperature depending on the thermal conductivity of the material in contact (See SI for more details).

To account for the possible influence of strain in the graphene induced by the SThM tip on the thermoelectric response we have varied the force exerted by the tip on the sample by changing the set point of the STGM. No change of the thermoelectric response with decreasing or increasing force was observed (unless the set point was chosen such that the tip did not contact the sample anymore), suggesting that the contact strain does not have an outsized effect on the measurements. Offsets introduced by the amplifier are accounted for by subtracting the background signal far away from the sample from the whole map.

Deconvolution. The Deconvolution is performed using a regularized filter algorithm rather than one based on the more straight forward polynomial division, as the latter can become numerically unstable for large denominator coefficients. The filter used is a constrained least-squares filter, which aims to minimize the difference between the ideal and the restored image while keeping the high frequency and thereby noise component to a minimum [46, 47]. The point-spread function used for deconvolution is the derivative of the Gaussian temperature distribution (Figure 3c and SI), and a Laplacian operator is used as the regularization operator to retain image smoothness.

Acknowledgments

OVK acknowledges the GrapheneCore3 grant number 881603 (Graphene Flagship), EU project QUANTIHEAT (Grant 604668), EPSRC project EP/K023373/1, UKRI project NEXGENNA and Paul Instrument Fund, c/o The Royal Society. P.G. acknowledges a Marie Skłodowska-Curie Individual Fellowship under Grant TherSpinMol (ID: 748642) from the European Union’s Horizon 2020 research and innovation programme. CE acknowledges a Marie Skłodowska-Curie Individual Fellowship under Grant NOSTA (ID: 704280) and EPSRC Grant EP/N017188/1.

References

- [1] Zhang Q, Sun Y, Xu W and Zhu D 2014 *Advanced Materials* **26** 6829–6851 ISSN 15214095 URL <http://doi.wiley.com/10.1002/adma.201305371>
- [2] Crossno J, Shi J K, Wang K, Liu X, Harzheim A, Lucas A, Sachdev S, Kim P, Taniguchi T, Watanabe K, Ohki T A and Fong K C 2016 *Science* **351** 1058–1061 URL <http://science.sciencemag.org.ezproxy.stanford.edu/content/351/6277/1058.abstract>
- [3] Harzheim A, Koenemann F, Gotsman B, van der Zant H and Gehring P 2020 *In print*
- [4] Kraemer D, Hu L, Muto A, Chen X, Chen G and Chiesa M 2008 *Applied Physics Letters* **92** 243503 ISSN 00036951 URL <http://aip.scitation.org/doi/10.1063/1.2947591>
- [5] Xia F, Mueller T, Golizadeh-Mojarad R, Freitage M, Lin Y M, Tsang J, Perebeinos V and Avouris P 2009 *Nano Letters* **9** 1039–1044 ISSN 15306984 URL <https://pubs.acs.org/doi/10.1021/nl8033812>
- [6] Guo S, Yang K, Zeng Z and Zhang Y 2018 *Physical Chemistry Chemical Physics* **20** 14441–14449 ISSN 14639076
- [7] Levander A X, Tong T, Yu K M, Suh J, Fu D, Zhang R, Lu H, Schaff W J, Dubon O, Walukiewicz

- W, Cahill D G and Wu J 2011 *Applied Physics Letters* **98** 012108 ISSN 00036951 URL <http://aip.scitation.org/doi/10.1063/1.3536507>
- [8] Lyeo H K, Khajetoorians A A, Shi L, Pipe K P, Ram R J, Shakouri A and Shih C K 2004 *Science* **303** 816–818 ISSN 00368075
- [9] Zhang Y, Hapenciuc C L, Castillo E E, Borca-Tasciuc T, Mehta R J, Karthik C and Ramanath G 2010 *Applied Physics Letters* **96** 062107 ISSN 00036951 URL <http://aip.scitation.org/doi/10.1063/1.3300826>
- [10] Mueller T, Xia F, Freitag M, Tsang J and Avouris P 2009 *Physical Review B - Condensed Matter and Materials Physics* **79** ISSN 10980121
- [11] Xu X, Gabor N M, Alden J S, Van Der Zande A M and McEuen P L 2010 *Nano Letters* **10** 562–566 ISSN 15306984 (Preprint 0907.3173) URL <https://pubs.acs.org/doi/pdf/10.1021/nl903451y>
- [12] Sun D, Aivazian G, Jones A M, Ross J S, Yao W, Cobden D and Xu X 2012 *Nature Nanotechnology* **7** 114–118 ISSN 17483395
- [13] Gabor N M, Song J C, Ma Q, Nair N L, Taychatanapat T, Watanabe K, Taniguchi T, Levitov L S and Jarillo-Herrero P 2011 *Science* **334** 648–652 ISSN 10959203
- [14] Zhang K, Yap F L, Li K, Ng C T, Li L J and Loh K P 2014 *Advanced Functional Materials* **24** 731–738 ISSN 1616301X URL <http://doi.wiley.com/10.1002/adfm.201302009>
- [15] Avsar A, Yang T Y, Bae S, Balakrishnan J, Volmer F, Jaiswal M, Yi Z, Ali S R, Guöntherodt G, Hong B H, Beschoten B and Özyilmaz B 2011 *Nano Letters* **11** 2363–2368 ISSN 15306984 URL <https://pubs.acs.org/doi/10.1021/nl200714q>
- [16] Goossens S, Navickaite G, Monasterio C, Gupta S, Piqueras J J, Pérez R, Burwell G, Nikitskiy I, Lasanta T, Galán T, Puma E, Centeno A, Pesquera A, Zurutuza A, Konstantatos G and Koppens F 2017 *Nature Photonics* **11** 366–371 ISSN 17494893 (Preprint 1701.03242)
- [17] Zuev Y M, Chang W and Kim P 2009 *Physical Review Letters* **102** ISSN 00319007 (Preprint 0812.1393)
- [18] Wei P, Bao W, Pu Y, Lau C N and Shi J 2009 *Physical Review Letters* **102** ISSN 00319007
- [19] Woessner A, Alonso-González P, Lundberg M B, Gao Y, Barrios-Vargas J E, Navickaite G, Ma Q, Janner D, Watanabe K, Cummings A W, Taniguchi T, Pruneri V, Roche S, Jarillo-Herrero P, Hone J, Hillenbrand R and Koppens F H 2016 *Nature Communications* **7** ISSN 20411723 (Preprint 1508.07864)
- [20] Shiao L L, Goh S C K, Wang X, Zhu M, Tan C S, Liu Z and Tay B K 2019 *IEEE Transactions on Nanotechnology* **18** 1114–1118 ISSN 19410085
- [21] Harzheim A, Spiece J, Evangeli C, McCann E, Falko V, Sheng Y, Warner J H, Briggs G A D, Mol J A, Gehring P and Kolosov O V 2018 *Nano Letters* **18** 7719–7725 ISSN 15306992 URL <https://pubs.acs.org/doi/10.1021/acs.nanolett.8b03406>
- [22] Gomès S, Assy A and Chapuis P O 2015 Scanning thermal microscopy: A review URL <http://doi.wiley.com/10.1002/pssa.201400360>
- [23] Haché A, Do P A and Bonora S 2012 *Applied Optics* **51** 6578–6585 ISSN 15394522
- [24] Shi Y, Dong X, Chen P, Wang J and Li L J 2009 *Physical Review B - Condensed Matter and Materials Physics* **79** ISSN 10980121
- [25] Wang Q H, Jin Z, Kim K K, Hilmer A J, Paulus G L, Shih C J, Ham M H, Sanchez-Yamagishi J D, Watanabe K, Taniguchi T, Kong J, Jarillo-Herrero P and Strano M S 2012 *Nature Chemistry* **4** 724–732 ISSN 17554330
- [26] Xue J, Sanchez-Yamagishi J, Bulmash D, Jacquod P, Deshpande A, Watanabe K, Taniguchi T, Jarillo-Herrero P and Leroy B J 2011 *Nature Materials* **10** 282–285 ISSN 14764660 (Preprint 1102.2642)
- [27] Tovee P, Pumarol M, Zeze D, Kjoller K and Kolosov O 2012 *Journal of Applied Physics* **112** 114317 ISSN 00218979 (Preprint 1110.6055) URL <http://aip.scitation.org/doi/10.1063/1.4767923>
- [28] Lee E J, Balasubramanian K, Weitz R T, Burghard M and Kern K 2008 *Nature Nanotechnology*

- 3** 486–490 ISSN 17483395
- [29] Sun D, Divin C, Berger C, De Heer W A, First P N and Norris T B 2010 *Physical Review Letters* **104** ISSN 00319007
 - [30] Ohta H, Kim S, Mune Y, Mizoguchi T, Nomura K, Ohta S, Nomura T, Nakanishi Y, Ikuhara Y, Hirano M, Hosono H and Koumoto K 2007 *Nature Materials* **6** 129–134 ISSN 14764660
 - [31] Rojo M M, Li Z, Sievers C, Bornstein A C, Yalon E, Deshmukh S, Vaziri S, Bae M H, Xiong F, Donadio D and Pop E 2019 *2D Materials* **6** 011005 ISSN 20531583
 - [32] Yoon D, Son Y W and Cheong H 2011 *Physical Review Letters* **106** ISSN 00319007 (*Preprint* 1103.3147)
 - [33] Lu H, Chu P K and An Z 2020 *Small* 1907170 ISSN 1613-6810 URL <https://onlinelibrary.wiley.com/doi/abs/10.1002/sml.201907170>
 - [34] McCann E and Koshino M 2013 *Reports on Progress in Physics* **76** ISSN 00344885 (*Preprint* 1205.6953)
 - [35] Castro Neto A H, Guinea F, Peres N M, Novoselov K S and Geim A K 2009 *Reviews of Modern Physics* **81** 109–162 ISSN 00346861 (*Preprint* 0709.1163)
 - [36] Nguyen M C, Nguyen V H, Nguyen H V, Saint-Martin J and Dollfus P 2015 *Physica E: Low-Dimensional Systems and Nanostructures* **73** 207–212 ISSN 13869477 (*Preprint* 1505.06474)
 - [37] Tovee P D, Pumarol M E, Rosamond M C, Jones R, Petty M C, Zeze D A and Kolosov O V 2014 *Physical Chemistry Chemical Physics* **16** 1174–1181 ISSN 14639076
 - [38] Vera-Marun I J, van den Berg J J, Dejene F K and van Wees B J 2016 *Nature Communications* **7** 11525 ISSN 2041-1723 URL <http://www.nature.com/doifinder/10.1038/ncomms11525>
 - [39] Harzheim A, Sowa J K, Swett J L, Briggs G A D, Mol J A and Gehring P 2020 *Physical Review Research* **2** 013140 (*Preprint* 1906.05401) URL <http://arxiv.org/abs/1906.05401>
 - [40] Gehring P, Van Der Star M, Evangeli C, Le Roy J J, Bogani L, Kolosov O V and Van Der Zant H S 2019 *Applied Physics Letters* **115** ISSN 00036951 (*Preprint* 1907.02815)
 - [41] Gehring P, Harzheim A, Spièce J, Sheng Y, Rogers G, Evangeli C, Mishra A, Robinson B J, Porfyraakis K, Warner J H, Kolosov O V, Briggs G A D and Mol J A 2017 *Nano Letters* **17** 7055–7061 ISSN 15306992 (*Preprint* 1710.08344) URL <http://pubs.acs.org/doi/abs/10.1021/acs.nanolett.7b03736>
 - [42] Menges F, Mensch P, Schmid H, Riel H, Stemmer A and Gotsmann B 2016 *Nature Communications* **7** 10874 ISSN 20411723 URL <http://www.nature.com/doifinder/10.1038/ncomms10874>
 - [43] Kim K, Jeong W, Lee W and Reddy P 2012 *ACS Nano* **6** 4248–4257 ISSN 19360851 URL www.acsnano.org
 - [44] Lee B, Kim K, Lee S, Kim J H, Lim D S, Kwon O and Lee J S 2012 *Nano Letters* **12** 4472–4476 ISSN 15306984 URL <http://pubs.acs.org/doi/10.1021/nl301359c>
 - [45] Evangeli C, Spiece J, Sangtarash S, Molina-Mendoza A J, Mucientes M, Mueller T, Lambert C, Sadeghi H and Kolosov O 2019 *Advanced Electronic Materials* **5** 1900331 ISSN 2199160X URL <https://onlinelibrary.wiley.com/doi/abs/10.1002/aelm.201900331>
 - [46] Hunt B R 1973 *IEEE Transactions on Computers* **C-22** 805–812 ISSN 00189340 URL <https://ieeexplore.ieee.org/stamp/stamp.jsp?tp=&arnumber=5009169>
 - [47] Lagendijk R L and Biemond J 2009 Basic Methods for Image Restoration and Identification *The Essential Guide to Image Processing* (Elsevier Inc.) pp 323–348 ISBN 9780123744579